Geoenvironmental Disasters

RESEARCH

Open Access

Experimental study on disaster mechanism of completely weathered granite landslide induced by extreme rainfall

Honghua Liu[1,3], Peng Yu[2,3*], Haitao Lu[2,3], Yongjian Xie[2,3], Zhongsheng Wang[2,3], Shengyou Hao[2,3], Hongjun Liu[1*] and Yunxia Fu[2,3]

Abstract

Background With the increased frequency of extreme weather, landslides induced by extremely heavy rainfall pose a major threat to human lives and property safety. In July 2020, a landslide occurred in the strongly weathered Laoshan Scenic Spot in Qingdao, China, and a short period of heavy rainfall was the main factor inducing the landslide.

Method Based on the similarity criterion, three groups of laboratory model tests under different extreme rainfall conditions were conducted using a large landslide model test box. The rainfall infiltration responses under different rainfall intensities, deformation processes, and failure modes of the slope were analyzed. The inducing mechanism and rainfall disaster process of granite landslides induced by extreme rainfall in strongly weathered areas were summarized.

Result The results showed that (1) a completely weathered granite landslide induced by rainfall had four stages, i.e., infiltration erosion, surface deformation, damage deepening, and overall instability, and the landslide was characterized by "sheet slip". (2) With greater rainfall intensities, the rainfall infiltration rate was higher, the changes in soil pressure, pore water pressure, water content, and matrix suction were faster, and the hysteresis effect was weaker. (3) A certain spatial distribution pattern was observed between slope deformation/damage and rainfall infiltration, and the research results could provide references for landslide warning and treatment in strongly weathered granite areas.

Keywords Extreme rainfall, Completely weathered granite slope, Landslide model test

Introduction

Landslide is the most common geological hazard. According to the Ministry of Natural Resources of China (M. N. R. 2022), 4772 geological disasters were recorded in China in 2021, of which 2335 landslides accounted for nearly half and posed a major threat to human lives and property safety. Factors inducing landslides mainly include internal conditions, such as landform, geotechnical type, and geological structure, and external forces, such as rainfall, earthquake, excavation, and excessive loading (Abedin et al. 2020).

Rainfall is a main external factor inducing landslides (Chen et al. 2021; Do et al. 2022). In recent years, rainfall has occurred with increasing frequency. In 2021 alone, 42

*Correspondence:
Peng Yu
13210276328@163.com
Hongjun Liu
hongjun@ouc.edu.cn
[1] Department of Environmental Science and Engineering, Ocean University of China, Qingdao 266100, People's Republic of China
[2] Key Laboratory of Geological Safety of Coastal Urban Underground Space, Ministry of Natural Resources, Qingdao 266100, People's Republic of China
[3] Qingdao Geo-Engineering Surveying Institute (Qingdao Geological Exploration Development Bureau), Qingdao 266100, People's Republic of China

rainfall events were recorded in China. The mechanism of landslide induced by rainfall is very complex (Liu and Wang 2021), often involving factors such as erosion, soil softening (Iqbal et al. 2018), seepage (Luo et al. 2022; Xu et al. 2022), stress redistribution (Tao et al. 2022), and multiple failure modes (Gu et al. 2023; Nguyen et al. 2022). In the process of rainwater infiltration into the slope, the water content and weight of the soil mass increase, generating the seepage force and pore water pressure in the slope (Huang et al. 2022). As the soil mass gradually reached saturation (Fig. 1), the anti-sliding force reduced while the sliding force increased, leading to the instability of the landslide mass (Zhang et al. 2022). Due to the vast uncertainty of natural slope materials, accurately quantifying the impact of rainfall on slope failures remains a major challenge, physical model test is still one of the most effective methods to study landslides. At present, landslide model tests mainly include seepage hydraulic model test (Miao et al. 2022a), bottom friction model test (Chang and Wang 2022), frame model test (Coppola et al. 2022), and geotechnical centrifuge model test (Miao et al. 2022b). The physical and mechanical action processes of the existing model need to be clarified to highlight the problems requiring further investigation. For example, Ma et al. (2016) carried out a landslide physical model test, obtained displacement, stress, and temperature information in landslide deformation and failure using multi-field information monitoring, and studied the space–time evolution law of the whole process of landslide failure. Chinkulkijniwat et al. (2019) established the relationship between the critical hydrological state, rainfall intensity, and soil properties according to the model test, analyzed the slope stability under the change of soil properties, slope, and rainfall intensity, and then determined the transformation of the depth of the failure surface. Miao et al. (2022a) selected the Liangshuijing landslide in the Three Gorges reservoir area for the centrifugal model test, revealing the failure mode and deformation mechanism under the coupling effects of water level fluctuation and rainfall.

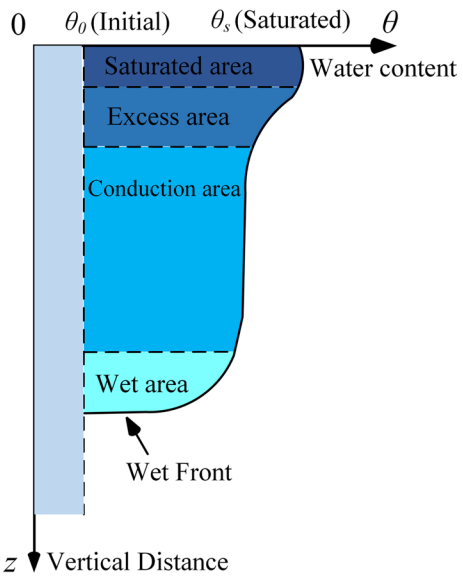

Fig. 1 Typical zones of rainfall infiltration process of landslide (Wang et al. 2019)

In addition, the nature of the soil mass is an important internal cause of landslides. Previous studies have found that the slip surface of granite landslides are mostly in the completely weathered zone with low shear strength, where the granite has been completely weathered into gravelly clay with poor engineering mechanical conditions (Sandeep et al. 2022). Under heavy rainfall, the soil mass softens, leading to slope instability (Ietto et al. 2016; Thiery et al. 2019). For example, Liu et al. (2020) took Weber's criterion as the rainfall similarity standard, introduced the hydromechanical similarity principle to conduct model tests, and analyzed the response law of the Pearl River completely weathered granite slope to rainfall infiltration. Hu et al. (2021) studied the meso sliding law of the Xiamen granite residual soil slope model under heavy rainfall from a meso perspective. Feng et al. (2022) explored the mechanism of landslides in Beiling's strongly weathered area through an in-situ rainfall physical model test.

The current model test-based researches on rainfall-induced weathered granite landslides mostly conducted small-scale tests, leading to the following limitations. (1) Small-scale model tests have significant scale effects between the model and the slope due to the differences in stress levels. For larger scale models, the resultant stress level differences are smaller. (2) During model tests, the direction of gravity in the model differs from that of the simulated gravity field, leading to erroneous results. (3) Rainfall intensity is the main control factor in the current research, and most studies set rainfall intensities to light, moderate, and heavy rains without considering extreme rainfall events such as 50-year rains. Therefore, this study takes the Fanling landslide in a strongly weathered rock area as an example and carries out systematic analyses of its geological conditions and rainfall characteristics. On this basis, three groups of large-scale laboratory model tests under different rainfall conditions were conducted, and the rainfall infiltration responses, deformation processes, and failure modes of the slope under various conditions were analyzed. The mechanism of granite landslides induced by extreme rainfall in strongly weathered areas and the process of rainfall disasters were summarized to provide references for landslide warning and prevention in such areas.

Landslide description

The Fanling landslide is in Fanlingqian Village, Laoshan Scenic Area, Qingdao City. Its central position is 120°40′49.31″ E and 36°50′50.11″ N, and its geomorphic type is a low mountain area with tectonic denudation. The area is a sloping terrain with a gentle front and steep middle and rear parts (Fig. 2).

According to the field survey, the Fanling landslide is classified as a soil-like landslide, and the sliding surface is in the completely weathered granite zone (Fig. 3). With a

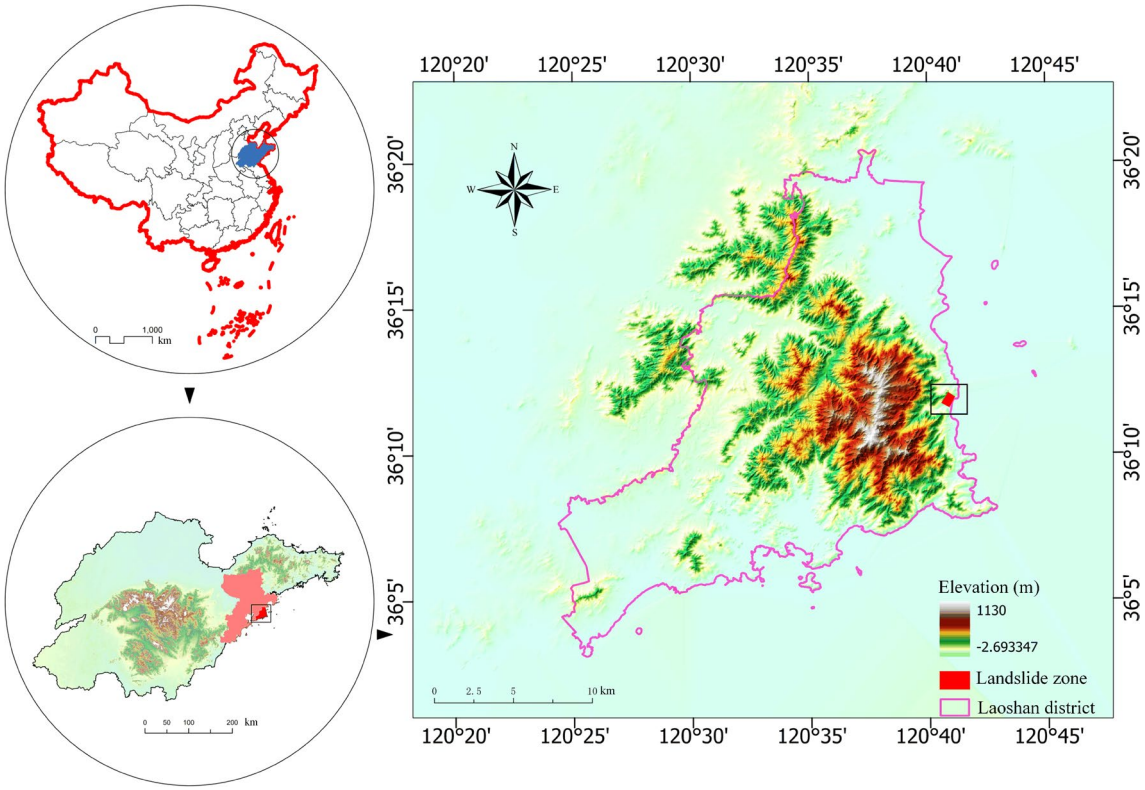

Fig. 2 Geographic location of Fanling landslide in 2020

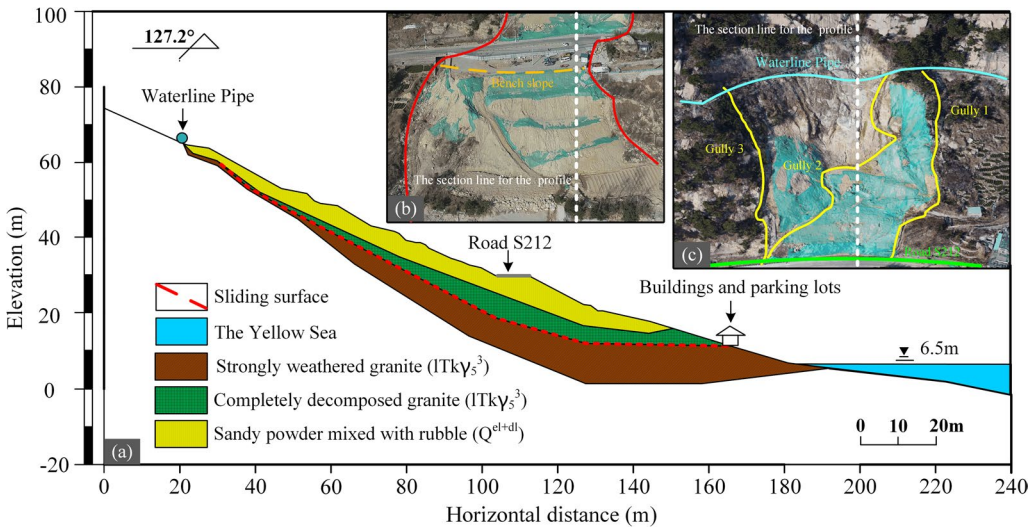

Fig. 3 **a** Schematic profile of landslide slope in 2020. **b**, **c** Overall view of slope

sliding mass covering a plane area of about 4.04×10^4 m^2, 12 m thick on average, and about 48.48×104 m^3 in volume, it is classified as a medium landslide. The front edge elevation is 3 to 5 m, 5 to 10 m from the sea surface. The rear edge elevation is 55 to 85 m, and the landslide width along the highway is 290 m. The overall slope of the landslide is steep, with an average gradient of 23°, and the slope direction and landslide direction are both 130° to 140°. The rear edge of the landslide is the boundary between bedrock and the Quaternary system, and the shear outlet is the boundary of the cataclastic deposit.

Completely weathered granite is sandy and fragile under pressure and prone to softening and disintegration during water penetration. It has high water permeability, and the original rock structure is difficult to identify. The Quaternary eluvial and colluvial deposits are 4.3 to 5.7 m thick, the completely weathered granite layer is 1.5 to 10.8 m thick, and the strongly weathered granite is 2 to 6.3 m thick.

In August 2007, the research area was hit by a 50-year rainstorm, and the slope collapsed (Fig. 4b), causing one death and washing away nearly 150 m of road. On July 23, 2020, the landslide slipped again (Fig. 4f) during another heavy rain, burying the tourist road (S212) at the foot of the slope, destroying the parking lot on the east side of the tourist road along with three parked cars, but fortunately causing no casualty.

Rainfall data suggest that precipitation in the region is mostly in June and August, accounting for 58% of the annual total. Before the 2007 and 2020 landslides, the rainfall continued for 6 days and 4 days, respectively. The daily rainfall on July 22, 2020 reached 175.96 mm, indicating that the 2020 landslide is a typical landslide induced by extreme rainfall (Fig. 5). With the landslide selected as the research object, the landslide model tests under extreme rainfall were carried out. This study is of great significance in revealing the evolution and mechanism of granite landslides induced by extreme rainfall in strongly weathered rock areas.

Materials and methods

Test instruments

The main sliding section with landslide cracks was selected as the test section, and the model tests ranged from the fully weathered granite pinch point to the shear outlet at the rear edge of the landslide, with a height of 75 m and a length of 210 m. The large-scale landslide model experiment device of the Key Laboratory of the Ministry of Education for Geological Hazards in the Three Gorges Reservoir Area was used for the tests (Fig. 6). The main body was a steel frame reinforced glass box 8 m long, 3.5 m high, and 0.8 m wide. To facilitate data collection and observation, the model box section was designed to be transparent with 5 cm × 5 cm grids. A constant head rainfall device was installed above the box to simulate different rainfall intensities. A hydraulic lifting system was installed under the box to flexibly simulate the natural slopes according to the terrain conditions of the landslide.

Fig. 4 Historical image map of landslide. **b** The shape of the first landslide occurred in August 2007 **f** The shape of the second landslide occurred in July 2020 (shot in September 2021). Others (**a**, **c**, **d**, **e**) are the historical image map of landslide in 2003, 2011, 2017 and April 2020

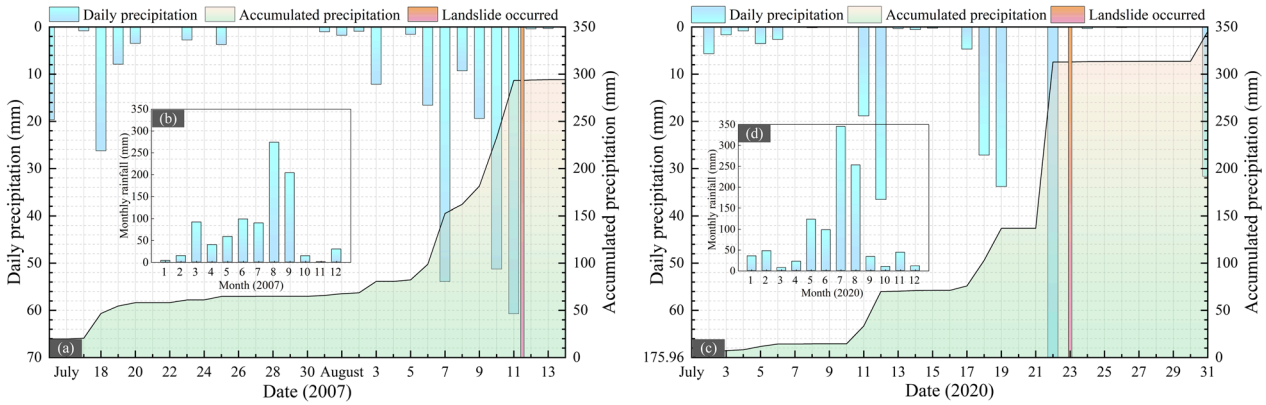

Fig. 5 Regional rainfall. **a** Rainfall time sequence diagram before landslide in 2007, **b** rainfall data in 2007, **c** rainfall time sequence diagram before landslide in 2020, **d** rainfall data in 2020

Fig. 6 **a**, **b** Model overview, **c** rainfall device

Test materials

According to the principles of geometric similarity, physical property similarity, and mechanical condition similarity, the geometric similarity ratio of the test model was determined as 1:30. The calculated physical parameters of the tests are shown in Table 1. The field investigation showed a low water content of the shallow surface layer of the landslide mass and highly similar water and soil characteristics between the surface residual soil and the completely weathered granite stratum. In addition, the rainfall mainly infiltrated the strongly weathered granite layer (impermeable interface) along the gaps, causing the landslide. Therefore, the surface residual soil and the completely weathered granite are considered the sliding mass during model tests.

According to the field investigation and in-situ sample test, analogous materials were selected, as shown in Fig. 7. The proportions of analogous materials in the landslide physical model were determined, and the mechanical and hydraulic properties of the analogous materials were tested (Table 2).

Table 1 Experimental model parameters and similarity ratios

Parameter	Prototype	Model tests	Scale
Length (m)	$l_p=210$	$l_m=7$	$C_l=l_p/l_m=30$
Density (kg/m^3)	$\rho_p=1900$	$\rho_m=1900$	$C_\rho=\rho_p/\rho_m=1$
Cohesion (kPa)	$c_p=19$	$c_m=0.63$	$C_c=c_p/c_m=30$
Friction	$\varphi_p=24$	$\varphi_m=24$	$C_\varphi=\varphi_p/\varphi_m=1$
Deformation modulus (GPa)	$E_p=5.4$	$E_m=0.18$	$C_E=E_p/E_m=30$
Poisson's ratio	$\mu_p=0.25$	$\mu_m=0.25$	$C_\mu=\mu_p/\mu_m=1$
Osmotic Coefficient (m/d)	$K_p=4$	$K_m=0.73$	$C_K=K_p/K_m=\sqrt{30}$
Rainfall intensity (mm/h)	q_p	q_m	$C_q=q_p/q_m=\sqrt{30}$
Rainfall time (h)	t_p	t_m	$C_t=t_p/t_m=\sqrt{30}$
Stress	σ_p	σ_m	$C_\sigma=\sigma_p/\sigma_m=30$
Displacement	u_p	u_m	$C_u=u_p/u_m=30$

Test method

After model material preparation with the benchmark mix proportion, the landslide physical model was constructed (Fig. 8).

(1) The sliding bed was established. As the actual sliding bed was strongly weathered granite with very low permeability, C30 cement concrete was used to build a right-angle wedge with a length of 7.84 m, a height of 2.46 m, and a slope of about 21° to simulate the impermeable strongly weathered granite layer, and the bottom layer was square bricks.

(2) The sliding surface was laid. A layer of kraft paper ($c_m=0.36$ kPa, $\phi_m=26°$) was first laid on the surface of the sliding bed. Then, a 1 to 2 cm soil layer of the sliding surface was laid from the rear edge of the landslide mass to the front edge in an imbricated manner. The layer was gradually thickened from the top to the toe of the slope. The thickness was determined using the grid lines on both sides of the model box, and the layer was compacted after laying.

(3) The sliding body was established. According to the geological profile map of the main sliding surface, the thickness of the sliding mass was reduced year-on-year. The thickness of the model was determined using the grid lines on both sides of the model box. The sliding mass soil was quantitatively allocated, laid, and compacted in layers, finally forming a complete landslide model body.

(4) Subsequently, the monitoring point layout was determined. The monitoring purpose was to observe the overall deformation and failure charac-

Fig.7 Landslide analogous materials

Table 2 Landslide analogous material proportioning

Location	Materials and scale									Mechanical and hydraulic properties		
										c_m (kPa)	φ_m (°)	K_m (m/d)
Sliding body	Stone grain (1–3 mm)	Fluvial sand	Barite sand	Clay	Carbonate of lime		Bentonite	Water		0.6–0.7	22–24	0.7–0.8
	48%	16%	16%	5%	5%		5%	5%				
Sliding surface	Glass bead (0.6–0.8 mm)		Glass bead (1.0–1.5 mm)			Slide body soil			Water	0.6–0.7	22–24	0.7–0.8
	40%		20%			30%			10%			
Sliding bed	Square brick, C30 cement concrete									–		

Fig. 8 Model building process **a** Sliding bed fabrication, **b** sliding surface production, **c** sliding body fabrication

teristics of the landslide during rainfall in real-time and analyze the impact of soil and water characteristics on the landslide failure during rainfall. A variety of data acquisition instruments and automatic camera monitoring systems were adopted in the tests. Three main monitoring surfaces were arranged at the front, middle, and rear edges of the slope, and two auxiliary monitoring surfaces were arranged at the front and middle sections. Vertical displacement sensors, tensiometers, and earth pressure sensors were embedded on the soil surface and soil bottom of the main monitoring surface. Pore water pressure sensors and moisture sensors were embedded on the soil surface and soil bottom of the main and auxiliary monitoring surfaces. Monitoring data were collected through automatic recorders. The arrangement is shown in Fig. 9.

(5) Finally, rainfall control was achieved. According to the hydrometeorological data of Laoshan Mountain, the annual average rainfall and maximum

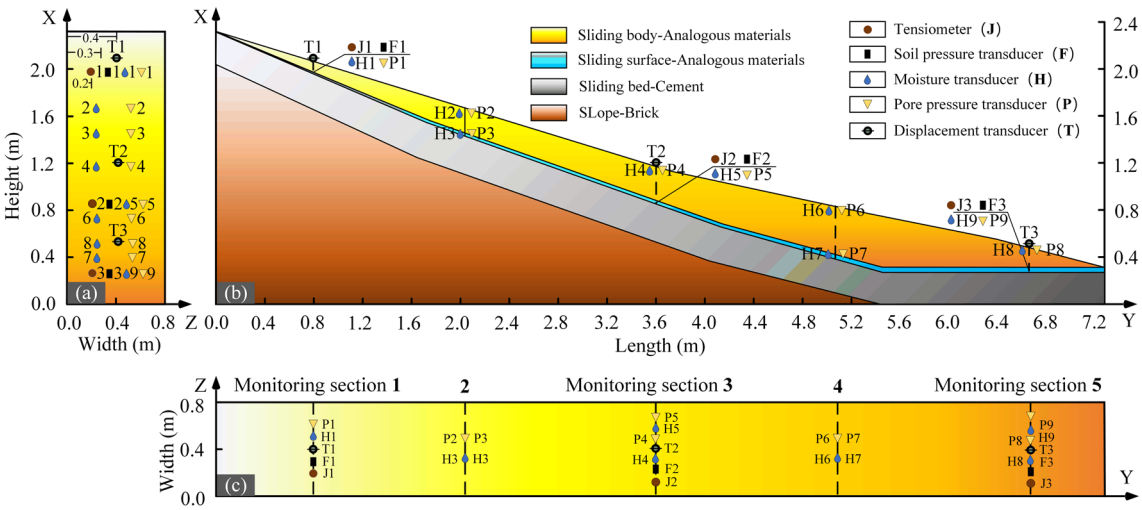

Fig. 9 Layout diagram of monitoring points

rainfall at the landslide location were statistically analyzed. The actual landslide site reached the rainfall intensity of 50 years on August 11, 2007, which was 64 mm/h. Rain continued for 21 h from 2:00 to 23:00 on July 22, 2020, reaching an accumulated rainfall of 175.96 mm. According to the principle of similarity ratio, the rainfall intensity was selected as the control factor to reproduce the 50-year rainfall conditions leading to landslides in 2020, and three extreme rainfall schemes were determined (Table 3), i.e., a 50-year rainstorm (N1), a heavy rainstorm (N2), and a rainstorm (N3).

The continuous rainfall mode was adopted in the test. The rainfall intensity control was mainly achieved by adjusting the pressure and flow of the water valve. Specifically, the rotation angle of the water valve was adjusted before the test to calibrate the initial rainfall intensity, and the rainfall uniformity was monitored with randomly arranged rain gauges. Under monitoring, the nozzle spray was gradually adjusted to ensure rainfall uniformity, and the rainfall intensity was back-calculated through the flow meter readings.

Results and discussion

Slope deformation

Figure 10 shows the time history curve of each displacement monitoring point under different rainfall conditions to analyze the slope deformation during rainfall.

(1) Under different rainfall intensities, the displacement change trend of each monitoring point was basically consistent. With the progress of rainfall, the rainwater infiltrated along the pores or microcracks, the physical strength of the landslide decreased, and the displacement began to increase. The slope underwent progressive deformation and failure. At the end of rainfall, the displacement reached the maximum and gradually stabilized. With higher rainfall intensities, the surface displacement was greater, and the time to reach the maximum was shorter. Under the 50-year rainfall (N1), the slope was unstable at about 0.5 h, and the displacement reached the maximum for about 0.9 h. Under heavy rain (N2), the slope was unstable at about 0.8 h, and the displacement reached the maximum in 1.1 h. However, under rainstorm (N3), the slope displacement does not reach the maximum value at the end of rainfall.

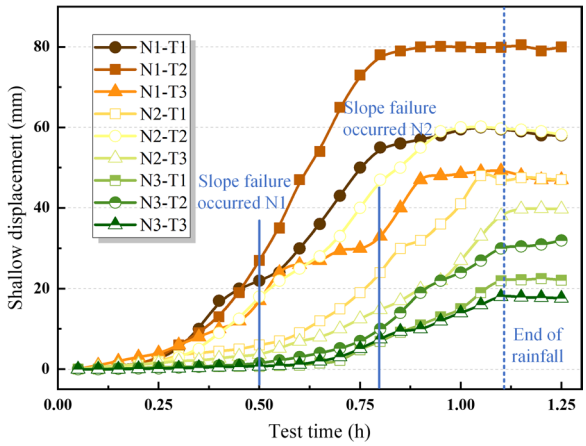

Fig. 10 Time history chart of surface displacement change under different rainfall intensity

(2) Under different rainfall intensities, the surface deformation had a certain lagging effect due to the different rainfall infiltration rates. With greater rainfall intensities, the deformation lagging time was shorter. The lagging effect of working conditions 1 to 3 was 0.2 h, 0.3 h, and 0.6 h, respectively.

(3) The spatial distribution pattern of deformation was analyzed. Under the same rainfall conditions, small deformation always appeared first at the foot of the slope before the rear and middle edges. When the slope was completely destroyed, the deformation rate of the middle edge decreased sharply, while the turning points of the deformation rates of the front and rear edges lagged behind. The middle edge (T2) had the largest deformation, followed by the trailing edge (T1), and the toe (T3) had the smallest deformation.

Table 3 Model rainfall program

	Rainfall intensity (mm/h)		Rainfall duration (h)		Total rainfall (mm)	
	Prototype	Model	Prototype	Model	Prototype	Model
N1	64	11.6	12	1.1	768	12.76
N2	20	3.6	12	1.1	240	3.96
N3	10	1.8	12	1.1	120	1.98

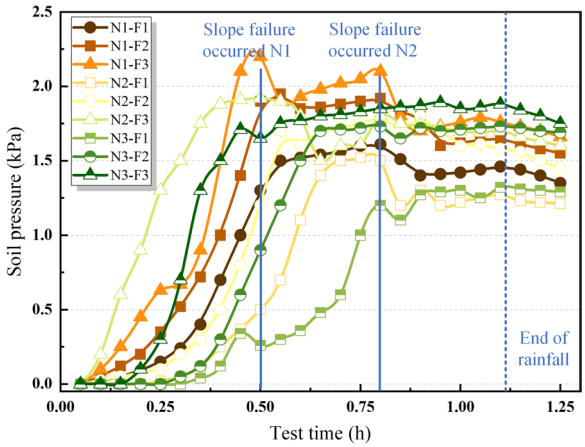

Fig. 11 Time history chart of soil pressure change under different rainfall intensity

Soil pressure

Figure 11 shows the time history curves at each soil pressure monitoring point under different rainfall conditions to analyze the response process of soil pressure to rainfall infiltration.

(1) The trends of soil pressure variation curves at each measuring point under different rainfall intensities were basically consistent and had good correspondence with the development of slope deformation and the change of pore water pressure. During rainfall, the soil mass was gradually saturated, the weight of the soil above the soil pressure sensors increased, and the soil pressure increased accordingly. Meanwhile, the slope surface expanded and shrunk, forming tension cracks acting as the dominant flow channels of rainwater infiltration, and further strengthening the seepage effect. After the rainfall, the water in the slope was discharged along the seepage channels, the soil weight decreased, and the soil pressure decreased slowly.

(2) According to slope deformation pattern analysis, gradual failures occurred, and the stress redistribution led to sudden stress changes. With the appearance of local and overall failures, vertical tensile failures occurred in the soil mass, and the earth pressure dropped suddenly. The sudden earth pressure drops appeared at the foot of the slope first, and the vertical earth pressure at the middle and rear parts began to decrease immediately afterward.

(3) Under greater rainfall intensities, the soil pressure changed faster due to water infiltration, and the trends were more apparent.

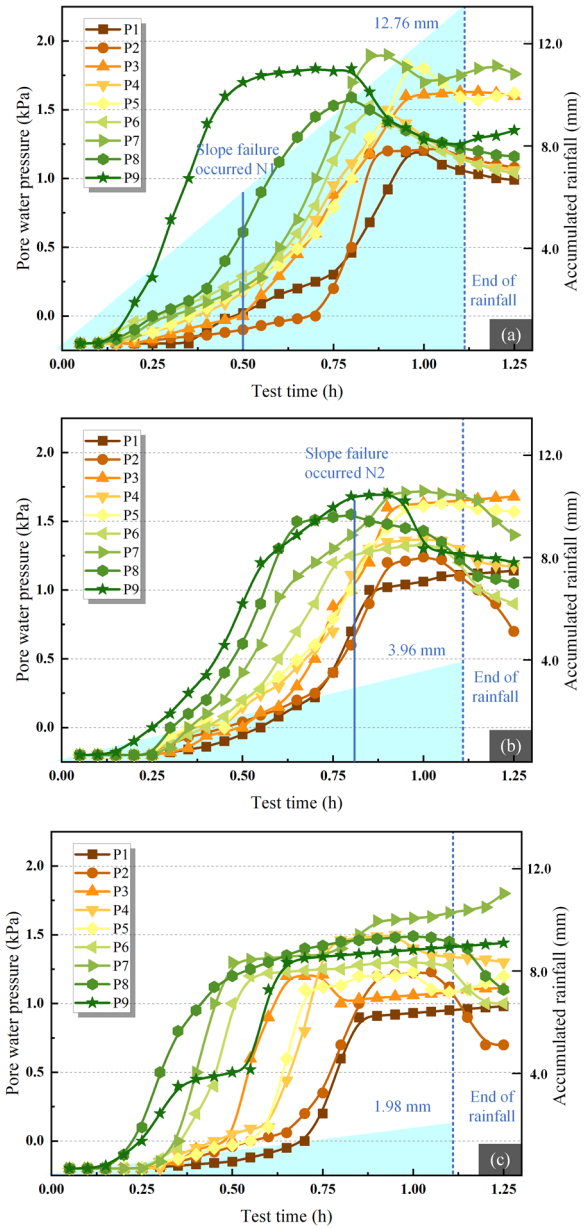

Fig. 12 Time history chart of pore water pressure change under different rainfall intensity **a** N1, **b** N2, **c** N3

Pore water pressure

Rainfall infiltration caused local saturation in the slope, changing the pore water pressure. Figure 12 shows the time history curves at each pore water pressure monitoring point under different rainfall conditions to analyze the response process of pore water pressure to rainfall infiltration.

(1) The changes in pore water pressure trends at each measuring point under different rainfall intensities

are basically consistent, with slow increases first, rapid increases next, and rapid decreases at last. At the beginning of the test, the pore pressure at some measuring points was negative. To explain this phenomenon, the pore water pressure sensor was pumped saturated (24 h) before the test, and the pore pressure was set to 0 under the condition of saturation and no water pressure. At the beginning of the test, the liquid–air interface between soil particles in unsaturated soil is a curved surface, and there is matrix suction. The theoretical expression of matrix suction is

$$s = u_a - u_w = \frac{2T_s}{R_s} \tag{1}$$

Where, s is matrix suction (kPa), u_a is pore gas pressure (kPa), u_w is pore water pressure (kPa), T_s is the liquid surface tension (kPa), R_s is the radius of curvature of the meniscus (m).

According to Eq. (1), the smaller the radius of curvature of the meniscus, the greater the matrix suction, and the smaller the corresponding pore water pressure. When the pore gas pressure is less than the matrix suction generated by the meniscus, the pore water pressure will have a negative value.

The soil moisture content gradually increased with the progress of rainfall. In the meantime, the seepage effect in the soil increased, and stable seepage channels gradually formed while the pore pressure slowly increased. Before the landslide, the soil mass underwent significant compression deformations, and excess pore water pressure was generated due to the untimely drainage, causing the surge of pore pressure. When the whole slope body was damaged, the pore water dissipated rapidly and the pore pressure decreased rapidly. At the end of rainfall, the seepage gradually stopped, the static pore water pressure gradually dissipated, and the pore pressure decreased.

(2) In terms of spatial pattern, the pore water pressure changes in different parts of the landslide at the same depth were different. The response time of the front edge (P8, P9) and middle part (P4, P5, P6, P7) of the landslide were short as the rainwater accumulated in the front and middle of the landslide, forming the groundwater level, and the pore pressure accumulated first.

(3) At the same monitoring profile, the variation of pore water pressure at different depths was also different. The variation history of water pressure in the shallow soil mass of the slope was closely related to the water seepage in the vertical cracks. The pore pressure variation range of the slope surface (P2, P4, P6, P8) was greater than that of the internal (P1, P3, P5, P7, P9). After the rainfall, the surface pore pressure decreased rapidly while the internal pore pressure continued to rise, with a hysteresis effect.

(4) In addition, higher rainfall intensities led to higher infiltration rates, greater seepage effects, and shorter soil saturation time, shortening the pore pressure response time and increasing the change rate.

Water content

Figure 13 shows the time history curves at each water content monitoring point under different rainfall conditions to analyze the response process of water content to rainfall infiltration.

(1) The trends of water content curves at each measuring point under different rainfall intensities were basically consistent, and the initial water content was 5.8% to 18.3%, with slow growth first, rapid growth next, and dynamic stability at last. Rainfall first infiltrated through the slope surface pores. As the wetting front reached the monitoring point, the volume moisture content increased. With the progress of rainfall, the tension cracks caused by slope deformation provided the dominant seepage channels for rainfall infiltration, rapidly increasing the internal water content of the landslide. It should be noted that the initial water content is controlled during the preparation of similar materials. However, the difference of initial water content is inevitable due to the different thicknesses at different locations of the slope during the preparation of the slide body.

(2) The infiltration speed at different locations of the slope varied, and the monitoring points at the rear edge and surface layer of the slope responded more quickly than those at the front edge and deep part of the slope. Among them, the water content of the rear edge points (H1, H2, H3) reached saturation sooner. The reason was the vertical infiltration of rainfall, and the rear edge of the landslide was steep and thin. The rear edge soon reached saturation under rainfall conditions and then infiltrated forward. It should be noted that the response law of slope water content and pore water pressure is inconsistent at the initial stage of the test. This is because with the rainfall, the rainwater collects in the front and middle of the landslide, forming the groundwater level, and the pore pressure accumulates first.

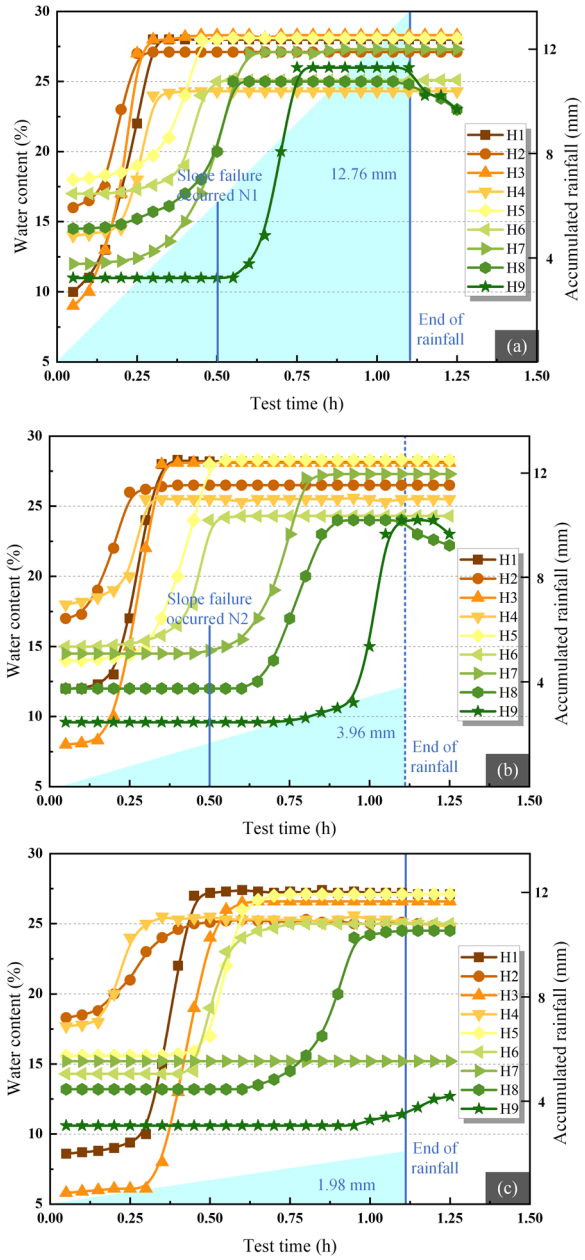

Fig. 13 Time history chart of water content change under different rainfall intensity **a** N1, **b** N2, **c** N3

(3) At the same monitoring section, the deep water content of the slope was significantly higher than that near the surface because the rainwater began to gather and finally saturate after reaching the slip zone (H1, H3, H5, H7, H9) through fissure infiltration. In the meantime, the slope surface (H2, H4, H6, H8) remained stable after the balance between downward infiltration and rainfall recharge was reached.

(4) With greater rainfall intensities, the increasing rate of water content was higher, and the time to reach the maximum water content was shorter.

(5) In addition, under the rainfall conditions of N1 and N2, the slope toe (H8, H9) decreased because the drainage path of the front edge of the landslide gradually increased, and the water storage capacity decreased under the effect of rain erosion.

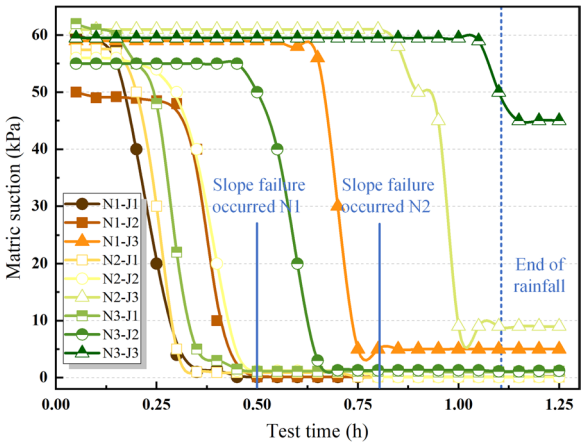

Fig. 14 Time history chart of matric suction change under different rainfall intensity

Matric suction

Figure 14 shows the time history curves of each water content monitoring point under different rainfall conditions. The response pattern of matrix suction to rainfall infiltration was similar to that of water content.

(1) The matric suction changed from stable to decreasing and then stabilizing with the rainfall. The response time of matrix suction and volume water content at the measuring point was relatively consistent, showing a negative correlation, i.e., the matrix suction decreased with the increase of volume water content. As the volume water content at the measuring point reached saturation, the matrix suction dissipated to 0 kPa.

(2) The matric suction at the top of the slope showed the fastest changes, followed by the middle of the slope, and the bottom responded the slowest. The matrix suction change rate increased with the increase in rainfall intensity.

Fig. 15 Landslide deformation process under condition N1 **a** 0.1 h, **b** 0.3 h, **c** 0.5 h, **d** 0.9 h

Fig. 16 Landslide deformation process under condition N2 **a** 0.1 h, **b** 0.3 h, **c** 0.9 h, **d** 1.1 h

Failure mode

Figures 15 and 16 show the landslide deformation processes under conditions N1 and N2, respectively. According to the model test results and the responses of each parameter to rainfall infiltration, the failure process of completely weathered granite induced by rainfall can be divided into four stages shown in Fig. 17.

(1) The infiltration erosion stage is shown in Fig. 17a. At the beginning of rainfall, the slope surface was saturated, and the soil surface was slightly eroded. The reasons for the erosion damage were twofold. One was that the kinetic energy generated by the falling raindrops caused splash and damage of the soil particles on the slope. The other was that the loose soil on the slope surface was washed away with the continuous infiltration of the slope, forming multiple erosion pits.

(2) The surface deformation stage is shown in Fig. 17b. As the rainfall continued, the loose materials accumulated on the slope were gradually washed away, and the high porosity of the strongly weathered soil

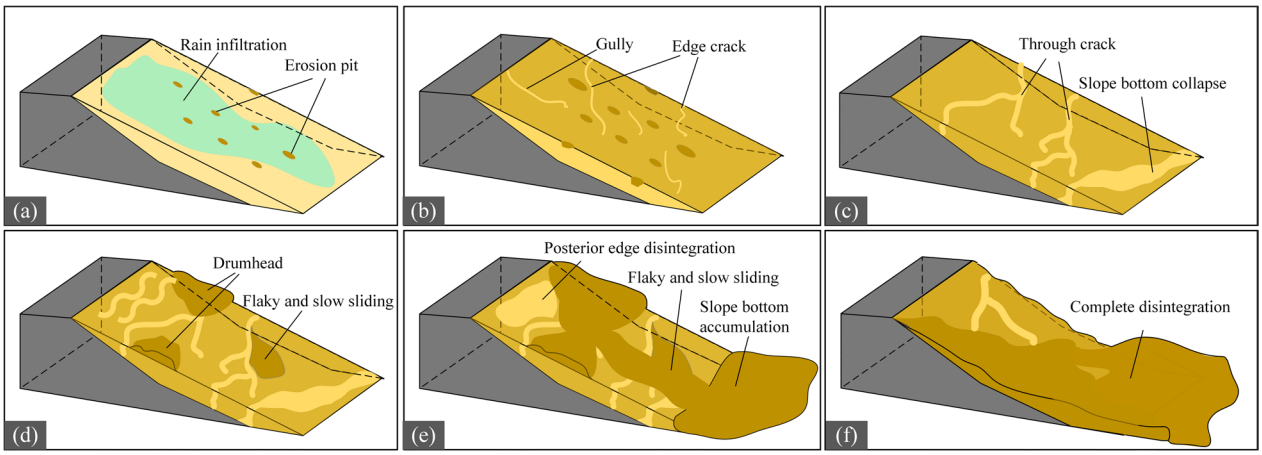

Fig. 17 Schematic diagram of failure process of completely weathered granite landslide under extreme rainfall

accelerated the water erosion and lateral erosion in the ditch. At the same time, the earth pressure and pore water pressure increased, the stress redistributed, and edge cracks and cracks formed at the positions of tensile stress concentration and continued to expand. The resulting dominant inflow seepage further strengthens the seepage effect.

(3) The damage-deepening stage is presented in Fig. 17c, d. With rainfall infiltration, the soil mass gradually saturated, and the interior of the slope started to destabilize, creeping toward the free surface. Under the combined action of rainwater scouring and seepage, the gully head at the toe of the front slope collapsed, and the side cracks and tension cracks of the slope gradually deepened and interconnected under tensile stress. As a result, the soil around the cracks softened further, the matrix suction dissipated, and the soil at the rear edge was affected by multiple tension cracks. The shear strength and effective stress were insufficient to offset the sliding force and cause soil flow damage. The middle and rear edges form a "drum-shaped bulge" under the load of the upper soil. At the same time, due to the different sliding speeds of the middle edge soil, "sheet sliding" appeared.

(4) The overall instability stage is shown in Fig. 17e, f. With continuous rainfall, the surface soil of the slope was almost saturated, especially after the saturation of the soil in the sliding zone, which provided a potential sliding surface for the landslide. In addition, the formation of the groundwater level exerted an uplifting force on the landslide soil, the anti-sliding force of the slope body decreased, and the slope body destabilized as a whole (Wang et al. 2019). The front and middle edges showed "sheet slip", which slowly accumulated at the foot of the slope in the form of "debris flow". The effective free face of the landslide appeared, and the rear edge disintegrated completely, resulting in overall pushing damage.

Conclusions

Based on the similarity theory, this study conducted large-scale landslide model tests with reasonably selected similar materials and sensors to study the failure mechanism of completely weathered granite landslides under extreme rainfall conditions and analyzed the response patterns of slope deformation, soil pressure, pore water pressure, water content, and matrix suction to rainfall infiltration. The main conclusions are as follows.

(1) Completely weathered granite landslides induced by rainfall were not rapid or sudden but divided into four stages, i.e., infiltration erosion, surface deformation, damage deepening, and overall instability. Under extreme rainstorm conditions, "sheet sliding" occurred at the front and middle edges of the slope, while the rear edge disintegrated, resulting in a pushing landslide as a whole.

(2) Under different rainfall intensities, the slope underwent asymptotic deformation and failure, and the surface deformation, soil pressure, pore water pressure, water content, and matrix suction changes had certain lagging effects. With greater rainfall intensities, the rainfall infiltration rate was higher, and the rainfall infiltration was more efficient. As a result, the soil pressure, pore water pressure, water content, and matrix suction changed faster, of which the hysteresis effect was weaker.

(3) A certain spatial distribution pattern was observed between slope deformation/damage and rainfall infiltration. Specifically, under the same rainfall conditions, the slope toe was the first to deform, and the rear and middle edges of the slope deformed later. The largest deformation was at the middle edge, followed by the rear edge, and the smallest deformation was at the slope toe. The response of pore water pressure in the front and middle of the slope was faster than that in the back, and the variation of the surface layer of the slope was greater than that of the interior. The response of water content and matrix suction in the rear edge and surface layer of the slope was faster than that in the front edge and deep part of the slope.

Author contributions

HS, LH (Hongjun Liu) and FY visited the landslide site and conducted the field survey. LH (Honghua Liu), PY and LH (Haitao Lu) contributed to model test. XY and WZ contributed to mapping. LH (Honghua Liu) and PY wrote the manuscript, edited and finalized the corrections. The final manuscript has been approved by all the authors. All authors read and approved the final manuscript.

Funding

The study was supported by Key Laboratory of Geological Safety of Coastal Urban Underground Space, Ministry of Natural Resources (Grant No. BHKF2021Z11) and Scientific Research Fund Project of Qingdao Geo-Engineering Surveying Institute (Grant No. 2022-QDDZYKY06).

Availability of data and materials

Data and materials are available upon request.

Declarations

Competing interests

The authors declare that they have no competing interests.

Received: 25 November 2022 Accepted: 30 January 2023
Published online: 22 February 2023

References

Abedin J, Rabby YW, Hasan I, Akter H (2020) An investigation of the characteristics, causes, and consequences of June 13, 2017, landslides in Rangamati District Bangladesh. Geoenviron Disasters 7(23):1–19. https://doi.org/10.1186/s40677-020-00161-z

Chang C, Wang G (2022) Creep of clayey soil induced by elevated pore-water pressure: implication for forecasting the time of failure of rainfall-triggered landslides. Eng Geol 296:106461. https://doi.org/10.1016/j.enggeo.2021.106461

Chen H, Qin S, Xue L, Xu C (2021) Why the Xintan landslide was not triggered by the heaviest historical rainfall: mechanism and review. Eng Geol 294:106379. https://doi.org/10.1016/j.enggeo.2021.106379

Coppola L, Reder A, Tarantino A, Mannara G, Pagano L (2022) Pre-failure suction-induced deformation to inform early warning of shallow landslides: proof of concept at slope model scale. Eng Geol 309:106834. https://doi.org/10.1016/j.enggeo.2022.106834

Chinkulkijniwat A, Tirametatiparat T, Supotayan C (2019) Stability characteristics of shallow landslide triggered by rainfall. J Mt Sci 16(9):2171–2183

Do NH, Goto S, Abe S, Nguyen KT, Miyagi T, Hayashi K, Watanabe O (2022) Torrent rainfall-induced large-scale karst limestone slope collapse at Khanh waterfall, Hoa Binh Province, Vietnam. Geoenviron Disasters 9(4):1–20. https://doi.org/10.1186/s40677-022-00206-5

Feng W, Hu R, Bai H (2022) Rainfall simulation study on formation mechanism of granite eluvium landslide. Sci Technol Eng 22(18):7799–7809 (**(in Chinese)**)

Gu X, Wang L, Ou Q, Zhang W (2023) Efficient stochastic analysis of unsaturated slopes subjected to various rainfall intensities and patterns. Geosci Front 14(1):101490. https://doi.org/10.1016/j.gsf.2022.101490

Hu H, Wu X, Zhang Y (2021) Failure mode analysis of granite residual soil slope based on rainfall landslide simulation test. J Xiamen Univ (nat Sci Ed) 60(06):1098–1102. https://doi.org/10.6043/j.issn.0438-0479.202004031(inChinese)

Huang W, Loveridge F, Satyanaga A (2022) Translational upper bound limit analysis of shallow landslides accounting for pore pressure effects. Comput Geotech 148:104841. https://doi.org/10.1016/j.compgeo.2022.104841

Ietto F, Perri F, Cella F (2016) Geotechnical and landslide aspects in weathered granitoid rock masses (Serre Massif, southern Calabria, Italy). CATENA 145:301–315. https://doi.org/10.1016/j.catena.2016.06.027

Iqbal J, Dai F, Hong M, Tu X, Xie Q (2018) Failure mechanism and stability analysis of an active landslide in the Xiangjiaba Reservoir Area, Southwest China. J Earth Sci 29:646–661. https://doi.org/10.1007/s12583-017-0753-5

Liu G, Li C, Lu B (2020) Experimental study on rainfall-induced shallow instability model of fully-strongly weathered rock slopes. J Changjiang Acad Sci 37(07):88–95+104. https://doi.org/10.11988/ckyyb.20190217. (**in Chinese**)

Liu X, Wang Y (2021) Probabilistic simulation of entire process of rainfall-induced landslides using random finite element and material point methods with hydro-mechanical coupling. Comput Geotech 132:103989. https://doi.org/10.1016/j.compgeo.2020.103989

Luo S, Huang D, Peng J, Tomás R (2022) Influence of permeability on the stability of dual-structure landslide with different deposit-bedding interface morphology: the case of the three Gorges Reservoir area, China. Eng Geol 296:106480. https://doi.org/10.1016/j.enggeo.2021.106480

Ma J, Tang H, Hu X (2016) Model testing of the spatial–temporal evolution of a landslide failure. Bull Eng Geol Env 76(1):1–17. https://doi.org/10.1007/s10064-016-0884-4

Miao F, Wu Y, Török Á, Li L, Xue Y (2022a) Centrifugal model test on a riverine landslide in the Three Gorges Reservoir induced by rainfall and water level fluctuation. Geosci Front 13(3):101378. https://doi.org/10.1016/j.gsf.2022a.101378

Miao F, Zhao F, Wu Y, Li L, Xue Y, Meng J (2022b) A novel seepage device and ring-shear test on slip zone soils of landslide in the Three Gorges Reservoir area. Eng Geol 307:106779. https://doi.org/10.1016/j.enggeo.2022.106779

Ministry of Natural Resources of the People's Republic of China. https://www.mnr.gov.cn/dt/ywbb/202201/t20220113_2717375.html. Accessed 13 Jan 2022

Nguyen TS, Yang K, Wu Y, TengF CW, Lee W (2022) Post-failure process and kinematic behavior of two landslides: case study and material point analyses. Comput Geotech 148:104797. https://doi.org/10.1016/j.compgeo.2022.104797

Sandeep CS, He H, Senetakis K (2022) Experimental and analytical studies on the influence of weathering degree and ground-environment analog conditions on the tribological behavior of granite. Eng Geol 304:106644. https://doi.org/10.1016/j.enggeo.2022.106644

Tao H, Zhang M, Gong L, Shi X, Wang Y, Yang G, Lei S (2022) The mechanism of slope instability due to rainfall-induced structural decay of earthquake-damaged loess. Earthq Res Adv 2(3):100137. https://doi.org/10.1016/j.eqrea.2022.100137

Thiery Y, Lacquement F, Marçot N (2019) Landslides triggered in weathered crystalline rocks of moderate latitudes: a case study in Mediterranean environment (The Maures Massif, France). Eng Geol 248:164–184. https://doi.org/10.1016/j.enggeo.2018.12.002

Wang R, Xia R, Xu W (2019) Study on physical simulation of rainfall infiltration process of landslide accumulation body. Adv Eng Sci 51(4):47–54. https://doi.org/10.15961/j.jsuese.201900295. (**in Chinese**)
Xu J, Ueda K, Uzuoka R (2022) Numerical modeling of seepage and deformation of unsaturated slope subjected to post-earthquake rainfall. Comput Geotech 148:104791. https://doi.org/10.1016/j.compgeo.2022.104791
Zhang S, Sun P, Jian R, Wang H, Xin P, Wang T (2022) Successful emergency evacuation from a catastrophic loess landslide reactivated by the torrential rain in October 2021 in Tianshui, Ganusu, NW China. Geoenviron Disasters 9:19. https://doi.org/10.1186/s40677-022-00222-5

Publisher's Note